PCCP

ROYAL SOCIETY OF CHEMISTRY

PAPER

View Article Online
View Journal | View Issue



Cite this: *Phys. Chem. Chem. Phys.*, 2025, **27**, 13662

# Modeling nitric oxide and its dimer: force field development and thermodynamics of dimerization†

Tijin H. G. Saji, [ab] Thijs J. H. Vlugt, [c] Sofia Calero [a] and Behnaz Bagheri *[ab]

Nitric oxide, NO, is a free radical that forms dimers, $(NO)_2$, at its vapor–liquid coexisting temperatures. In this work, we developed an all-atom force field for NO and $(NO)_2$. To assess the performance of this force field, we computed the vapor–liquid equilibrium (VLE) properties of the reactive NO–$(NO)_2$ system, as well as those of pure NO and pure $(NO)_2$, using Continuous Fractional Component Monte Carlo (CFCMC) simulations. We then compared the results with the available experimental data and predictions from two previously developed force fields. For the reactive NO–$(NO)_2$ system, we performed CFCMC simulations in the reactive Gibbs ensemble in which the formation of NO dimers, $2NO \rightleftharpoons (NO)_2$, is considered. The predicted coexistence vapor–liquid densities, dimer mole fractions in the liquid phase, saturated vapor pressures, and heats of vaporization using our force field in the temperature range 120 K to 170 K are in excellent agreement with experimental values. In addition, we conducted a systematic parameter study to analyze the sensitivity of the new force field parameters and the isolated molecule partition functions of $(NO)_2$ on the VLE properties of the reactive NO–$(NO)_2$ system. The results indicate that the VLE properties of the reactive NO–$(NO)_2$ system are affected by both the force field parameters of the involved species as well as the isolated molecule partition functions of $(NO)_2$.

Received 27th February 2025,
Accepted 8th June 2025

DOI: 10.1039/d5cp00784d

rsc.li/pccp



## 1 Introduction

Electric gas discharge plasmas generated in $O_2$ and $N_2$ containing gases are sources of producing considerable amounts of nitric oxide (NO) radicals.[4,5] The molecule NO serves as a precursor for production of other reactive nitrogen species such as nitrogen dioxide ($NO_2$), dinitrogen trioxide ($N_2O_3$), dinitrogen tetraoxide ($N_2O_4$), nitrites ($NO_2^-$), nitrates ($NO_3^-$), peroxynitrite ($ONOO^-$), peroxynitrous acid (ONOOH), and others, either directly in the gas phase plasma or upon absorption in aqueous solutions.[6,7] NO and its byproducts play a key role in plasma processing of liquids and biological materials for applications in biomedicine[8–10] and agriculture.[11–13] Biomedical applications of plasmas are based on the selective delivery of reactive oxygen and nitrogen species to living tissues for the treatment of chronic wounds and skin infections, and in oncology.[14,15] In plasma-agriculture, a specific mixture of reactive oxygen and nitrogen species, directly or dissolved in water,

[a] *Department of Applied Physics and Science Education, Technical University of Eindhoven, PO Box 513, Eindhoven, 5600 MB, The Netherlands. E-mail: b.bagheri@tue.nl*
[b] *Institute for Complex Molecular Systems, PO Box 513, Eindhoven, 5600 MB, The Netherlands*
[c] *Process & Energy Department, Faculty of Mechanical, Maritime and Materials Engineering, Delft University of Technology, Leeghwaterstraat 39, Delft, 2628 CB, The Netherlands*

† Electronic supplementary information (ESI) available: Experimental values for bond distances and angles of NO and $(NO)_2$ are presented in Table S1. The experimental rotational constants and vibrational frequencies of NO and its dimer are presented in Tables S2 and S3, respectively. The values of the isolated molecule partition functions for NO and $(NO)_2$ for different temperatures are presented in Table S4. The VLE properties of the reactive NO–$(NO)_2$ system predicted using the New FF as well as the respective experimental values are presented in Tables S5–S7. The force field parameters developed by Zhou *et al.*[38] (Zhou FF) and Lachet *et al.*[36] (Lachet FF) are listed in Table S9. The critical temperature, density, and pressure of pure NO and $(NO)_2$ using the New FF, the Zhou FF, and the Lachet FF are listed in Table S10. The critical temperatures and densities of NO–$(NO)_2$ systems for various values of $D_{0,(NO)_2}$ are listed in Table S11. The twelve different force field parameters used for our parameter study are listed in Table S12 with the respective predicted critical temperatures and densities in Table S13. Fig. S1 shows the vapor–liquid coexistence densities obtained with the the New FF along with the extrapolated densities at temperatures close to the critical temperature obtained by fitting the vapor and liquid phase densities to the law of rectilinear diameters. Fig. S2 and S3 show the changes in the orthobaric densities and dimer mole fractions using the different values of $D_{0,(NO)_2}$ listed in Table S10. Fig. S4–S33 show the variations in the coexistence densities, dimer mole fractions, saturated vapor pressures, heats of vaporization and total enthalpies of the reactive NO–$(NO)_2$ system for the different force fields used for our parameter study. Fig. S34 and S35 show the difference in the area of the attractive L-J potential energy for systems with different values of $\varepsilon$ and $\sigma$, respectively. See DOI: https://doi.org/10.1039/d5cp00784d

 

is used as fertilizer and/or pesticide for the growth of plants.[16–18] For these applications, it is crucial to quantify the amount of plasma species that are absorbed by aqueous solutions from the gas phase plasmas. Macroscopic models of plasma–liquid systems are commonly used to predict the densities of species in the gas phase plasma and in the aqueous phase.[19–23] In these models, the transfer of plasma species from the gas phase into aqueous solutions is incorporated using solubility coefficients of individual species. The solubility coefficients of individual plasma species are commonly used to interpret experimental findings.[6,7] Experimental solubility coefficients, however, are only available for a few species and solutions, and with limited accuracy. This limits the predictive power of macroscopic models in determining the concentrations of plasma species in the aqueous phase.[24] Molecular simulations are a natural choice to compute the solubility coefficients of plasma species. We aim to use force field-based molecular simulations to compute the solubility coefficients of NO species. It is important to note that the accuracy of force field-based molecular simulations depends on the quality of the force fields used to describe the solute species in the gas phase, the properties of aqueous solutions, and their interactions.[25] To the best of our knowledge, there are no all-atom force field parameters for NO that can predict its vapor–liquid-equilibrium (VLE) properties in agreement with available experimental results. This motivated us to first develop a predictive all-atom force field for NO. In a future study, we plan to focus on interaction mechanisms of NO species with aqueous solutions and computing its solubility coefficients.

NO has an unpaired electron in the molecular orbital $\pi^*$ that is delocalized between the N and O atoms.[26] NO tends to make dimers, trimers, and higher order oligomers with itself; the extend of which depends on temperature and pressure.[27,28] Kohler[29] reported that in the liquid phase, the existence of dimers is predominant, while the gas phase is mostly comprised of monomers. Marinakis *et al.*[28] also reported that the liquid phase consists predominantly of dimers, but the presence of higher oligomers may also be possible. The mole fraction of dimers in the liquid phase decreases with increasing temperature as studied by Walsh *et al.*,[30] Kohler,[29] and Marinakis *et al.*[28] According to Smith and Johnston,[31] the mole fraction of dimers in the liquid phase in the temperature range of 110–120 K, is in the range of 0.95–0.91. High-level quantum mechanical calculations indicate that the planar *cis*-ONNO configuration is the most stable form of the NO dimer, with the non-planar *trans*-ONNO lying about 50 kJ mol$^{-1}$ higher in energy.[32,33] However, Marinakis *et al.*,[28] suggested that non-planar NO dimers may still be present in the liquid phase. Therefore, the development of force field parameters for NO should account for dimer formation in the liquid phase.

Several force fields are available for NO.[28,34–38] The formation of NO dimers was considered in the force fields developed by Kohler,[34] Hirschfelder,[35] and Lachet *et al.*[36] using a single-site model for NO and a two-site model for $(NO)_2$. The force field developed by Lachet *et al.*[36] can predict the experimental thermodynamic and transport properties of the reactive NO–$(NO)_2$ system better than the force fields developed by Kohler[34] and Hirschfelder,[35] as shown in the original paper by Lachet *et al.*[36] As atomistic information is lacking in the force field developed by Lachet *et al.*,[36] due to the treatment of NO as a single-site model, this force field is not suitable for applications where the atomistic information of the N and O atoms in NO molecules is needed.[28] The force fields for NO developed by Marinakis *et al.*,[28] Yang *et al.*,[37] and Zhou *et al.*[38] are of all-atom type. In the work by Marinakis *et al.*,[28] the formation of NO dimer was implemented using additional attractive and repulsive Gaussian potential terms on top of van der Waals interactions, making it less compatible with widely used molecular simulation packages. Moreover, the transferability of the Gaussian potential to other systems, such as mixtures with water, is not well understood. For example, it remains unclear which mixing rules should be applied in such cases. The force field developed by Yang *et al.*[37] for NO does not take dimer formation into account. Furthermore, this model consists of a 9-6 Lennard-Jones potential with a sixth-order combination law, which is not readily implemented in all popular simulation engines. The force field for NO developed by Zhou *et al.*[38] only takes into account the non-bonded (electrostatic and van der Waals) interactions of the molecule. This force field was optimized to reproduce the experimental density and enthalpy of vaporization of liquid NO at its boiling point. However, it does not take into account the tendency of NO monomers to dimerize (*i.e.*, no dimers are formed in the model). Therefore, this force field is incapable of reproducing the experimental $(NO)_2$ mole fraction in the liquid phase.

In this work, we developed an all-atom force field for NO and its dimer, $(NO)_2$, which include 12-6 Lennard-Jones and Coulombic potential energy functions. We assumed that NO exists only as monomers and dimers, and dimers exist in a planar *cis*-ONNO configuration.[32] We computed the VLE properties of the reactive NO–$(NO)_2$ system (*e.g.*, coexistence densities, dimer mole fractions in liquid phase, saturated vapor pressures, and heats of vaporization) using continuous fractional component Monte Carlo (CFCMC) simulations in the reactive Gibbs ensemble.[39–44] The VLE properties of the reactive NO–$(NO)_2$ system computed using our force field parameters are in excellent agreement with the experimental values. The performance of our newly optimized force field is also compared with two existing force fields, Lachet *et al.*[36] and Zhou *et al.*,[38] that have been used extensively.[45–48]

The rest of the manuscript is organized as follows. The CFCMC simulations are described in Section 2. In Section 3, the details of the new force field parameters are provided. The isolated molecule partition functions for NO and $(NO)_2$ are discussed in Section 4. The validation of the new force field with the experimental VLE properties and the comparison of the force field with existing NO force fields is investigated in Section 5. In Section 5 the sensitivity of the VLE properties on the isolated molecule partition functions of the dimer and the Lennard-Jones potential parameters is discussed. Finally, concluding remarks are provided in Section 6.

## 2 Methodology

CFCMC simulations[49–51] using the open-source Brick-CFCMC software[51–53] were used to assess the validity of our force field parameters for NO and $(NO)_2$ compared to experimental findings. We performed a series of systematic CFCMC simulations in the reactive Gibbs ensemble (RGE)[39–44] at constant temperature, number of atoms, and volume, to reproduce the experimental vapor–liquid coexistence densities, coexistence pressures, dimer mole fractions, and heats of vaporization of the reactive NO–$(NO)_2$ system for the temperature range of 121.5 K to 165 K. From these, the critical temperature, density, and pressure of the system were calculated. RGE is a combination of the Gibbs ensemble (GE),[54,55] which consists of two simulation boxes, one for each of the vapor and liquid phases to model the VLE, and the reaction ensemble,[39,42,43] which in our case models the following equilibrium reaction

$$2NO \rightleftharpoons (NO)_2. \tag{1}$$

We also performed CFCMC simulations in the single-component Gibbs ensemble (GE)[56,57] at constant temperature, number of molecules, and volume to compare the performance of our force field with the force fields developed by Lachet *et al.*[36] and Zhou *et al.*[38] To do this, we computed the coexistence densities and pressures of pure NO for the temperature range 120 K to 170 K and pure $(NO)_2$ for the temperature range 120 K to 300 K.

In CFCMC simulations, fractional molecules (compared to normal or ''whole'' molecules) are introduced whose interactions with the rest of the molecules in the system are modulated by a continuous coupling parameter $\lambda$. The value of $\lambda$ ranges from 0 to 1. $\lambda = 0$ means that the fractional molecules act as ideal gas molecules and do not have interactions with the rest of the molecules in the system. $\lambda = 1$ represents ''whole'' molecules that can fully interact with the other molecules. A fractional group is a collection of one or more fractional molecules. The fractional group must be charge neutral.[51–53] To increase the efficiency of molecule transfers (insertions/deletions), the Wang–Landau algorithm[58] is used to bias the coupling parameter $\lambda$ with a weight function $W(\lambda)$. This ensures a flat observed probability distribution of $\lambda$, therefore making sure that the sampling issues due to the energy barriers in $\lambda$ space are not encountered. In our simulations, we used 100 bins to obtain a histogram for values of $\lambda$ and their probability of occurrence $p(\lambda)$. The Boltzmann average of an observable ($A$) is then computed using[59]

$$\langle A \rangle = \frac{\langle A \exp[-W(\lambda)] \rangle_{\text{biased}}}{\langle \exp[-W(\lambda)] \rangle_{\text{biased}}}. \tag{2}$$

For the RGE, there are two sets of fractional groups;[59] (1) fractional group for individual components/molecules involved in the system for molecule transfers and (2) fractional group for reactions. The contributions of fractional components are not taken into account when computing the ensemble averages.[59]

The fractional group for molecule transfers facilitates molecule transfers between the vapor and liquid simulation boxes. The reactive NO–$(NO)_2$ system contains two such fractional groups, one each for NO and $(NO)_2$. As mentioned earlier, the strength of the interactions of the molecules in these group are modulated by their corresponding $\lambda$ values ($\lambda_{\text{Gibbs,NO}}$ and $\lambda_{\text{Gibbs,}(NO)_2}$). There are three trial moves associated with the fractional molecules for molecule transfers:[59,60] (1) attempts to change the value of $\lambda_{\text{Gibbs}}$; (2) attempts to transfer a fractional molecule from one simulation box to another; (3) attempts to convert a fractional molecule in a box to a ''whole'' molecule, and simultaneously, transform a ''whole'' molecule in the other box into a fractional molecule.

For the NO–$(NO)_2$ system, the fractional group for reactions contains fractional molecules of either the reactants (2NO) or the reaction products $(NO)_2$. The interactions of these molecules with the other molecules in the simulation is modulated by the parameter, $\lambda_{\text{reaction}}$. One fractional group for reactions was added each to the liquid and vapor simulation boxes. The trial moves associated with the fractional molecules in this group are:[61] (1) attempts to change the value of $\lambda_{\text{reaction}}$; (2) attempts to convert the fractional molecules of reactant to fractional molecules of reaction product, or *vice versa*; (3) attempts to convert the fractional molecules of the reactant (or the reaction product) in a box to ''whole'' molecules of the reaction product (or the reactant), and simultaneously, transform ''whole'' molecules of the reaction product (or the reactant) to fractional molecules of reactant (or the reaction product).

The GE simulation of unreactive NO and $(NO)_2$ systems contains the fractional group for molecule transfers and not the fractional group for reactions. In addition to the trial moves associated with the fractional molecules present in the RGE and the GE simulations, both the simulation setups have thermalization trial moves (molecule translations, rotations and volume changes). Since the molecules in the simulation are rigid, the sampling of the intramolecular degrees of freedom are not considered.

The simulation in the RGE is considered equilibrated when a combined phase equilibrium and chemical equilibrium is achieved. The two simulation boxes in this ensemble can exchange molecules and volume until the two phases reach phase equilibrium. Phase equilibrium is achieved when the liquid and vapor chemical potentials, $\mu$, of individual species are equal ($\mu_{\text{NO,liquid}} = \mu_{\text{NO,vapor}}$ and $\mu_{(NO)_2,\text{liquid}} = \mu_{(NO)_2,\text{vapor}}$). The chemical potential in the phase $x$ (liquid or vapor) for the component $i$ (NO or $(NO)_2$) is given by[59]

$$\begin{aligned}\mu_{x,i} &= -k_B T \ln\left[\frac{V_x}{\Lambda_i^3 (N_{x,i}+1)}\right] \\ &\quad - k_B T \ln\left[\frac{p_{x,i}(\lambda_{\text{Gibbs},i}=1)}{p_{x,i}(\lambda_{\text{Gibbs},i}=0)}\right],\end{aligned} \tag{3}$$

where $k_B$ is the Boltzmann constant, $T$ is the temperature, $V_x$ is the volume of the simulation box that represents phase $x$, $\Lambda_i$ is the thermal de Broglie wavelength of component $i$, $N_{x,i}$ is the number of molecules of component $i$ in phase $x$. $p_{x,i}(\lambda_{\text{Gibbs},i} = 1)$

 

and $p_{x,i}(\lambda_{\mathrm{Gibbs},i} = 0)$ are the probabilities that $\lambda_{\mathrm{Gibbs},i}$ (coupling parameter of fractional molecule for molecule transfers for component $i$) are 1 and 0, respectively, in phase $x$. Chemical equilibrium is attained when $2\mu_{\mathrm{NO,liquid}} = \mu_{(\mathrm{NO})_2,\mathrm{liquid}}$ and $2\mu_{\mathrm{NO,vapor}} = \mu_{(\mathrm{NO})_2,\mathrm{vapor}}$.[62,63] For a system containing $S$ components in phase $x$, where components 1 to $R$ are reactants and $R + 1$ to $S$ are reaction products, the chemical potentials of the components follow the relations[42,52]

$$\sum_{i=1}^{R} \nu_i \mu_{i,x} = -k_B T \ln\left\langle \prod_{i=1}^{R} \left(\frac{q_i}{\Lambda_i^3 \rho_{i,x}}\right)^{\nu_i} \right\rangle - k_B T \ln\left[\frac{p_{i,x}(\lambda_{\mathrm{reaction},x} = 1)}{p_{i,x}(\lambda_{\mathrm{reaction},x} = 0)}\right], \quad (4)$$

$$\sum_{i=R+1}^{S} \nu_i \mu_{i,x} = -k_B T \ln\left\langle \prod_{i=R+1}^{S} \left(\frac{q_i}{\Lambda_i^3 \rho_{i,x}}\right)^{\nu_i} \right\rangle - k_B T \ln\left[\frac{p_{i,x}(\lambda_{\mathrm{reaction},x} = 1)}{p_{i,x}(\lambda_{\mathrm{reaction},x} = 0)}\right], \quad (5)$$

where, $q_i$ is the isolated molecular partition function (excluding the translational part) of component $i$, $\nu_i$ is the stoichiometric coefficient of component $i$ in the reaction, $\rho_{i,x}$ is the number density of the species $i$ in phase $x$. $p_i(\lambda_{\mathrm{reaction},x} = 1)$ and $p_i(\lambda_{\mathrm{reaction},x} = 0)$ are the probabilities that $\lambda_{\mathrm{reaction},x}$ (coupling parameter of fractional group for reactions for phase $x$) approaches 1 and 0, respectively, for component $i$.

For a two-component system such as NO–$(NO)_2$, which follows the reaction in eqn (1), (4) and (5) simplify to

$$\nu_i \mu_{i,x} = -k_B T \ln\left[\frac{q_i}{\Lambda_i^3 \rho_{i,x}}\right]^{\nu_i} - k_B T \ln\left[\frac{p_{i,x}(\lambda_{\mathrm{reaction},x} = 1)}{p_{i,x}(\lambda_{\mathrm{reaction},x} = 0)}\right], \quad (6)$$

where $i$ are the components NO and $(NO)_2$. From eqn (4)–(6) it is clear that to perform CFCMC simulations in the RGE, partition functions of the isolated molecules involved in the reaction are required. More discussion about the partition functions of NO and $(NO)_2$ are given in Section 4. The simulation in the GE is equilibrated when there is equilibrium between the vapor and liquid phases (phase equilibrium).

The critical temperatures and densities were obtained by fitting the liquid and vapor phase densities to the law of rectilinear diameters[64]

$$\frac{\rho_l + \rho_g}{2} = \rho_c + A(T - T_c), \quad (7)$$

$$\rho_l - \rho_g = B(T - T_c)^{\beta}, \quad (8)$$

where $\rho_l$ and $\rho_g$ correspond to the density of liquid and vapor phases, respectively, along the VLE curve, $\rho_c$ is the critical density, and $T_c$ is the critical temperature. $A$ and $B$ are system dependent fitting parameters. For the RGE, $\beta$ is selected as the value that corresponds to the maximum of the coefficient of determination ($R^2$) for the linear regression fit of $\left(\frac{\rho_l - \rho_g}{\rho_0}\right)^{\frac{1}{\beta}}$ *versus* temperature,[62] where $\rho_0$ is an arbitrary number density which is set to 1 Å$^{-3}$. In the single-component GE, $\beta$ is taken as 0.32.[65]

To compute the coexistence pressures of the RGE and the GE systems, a series of NPT simulations for vapor phase were performed to match the vapor phase densities of the RGE and the GE. The $P$–$T$ saturation points were fitted to a correlation of the form[61]

$$P_{\mathrm{sat}}(T) = A \exp\left[\frac{-B}{T}\right], \quad (9)$$

where $A$ and $B$ are system-dependent fitting parameters. The critical saturated vapor pressure, $P_c$, was obtained by extrapolating the above correlation to $T_c$.

The molar heat of vaporization was calculated as the difference between the average molar enthalpy of the vapor and liquid simulation boxes of the RGE[36]

$$\Delta h_{\mathrm{vap}} = h_{\mathrm{vapor}} - h_{\mathrm{liquid}}, \quad (10)$$

where $\Delta h_{\mathrm{vap}}$ is the molar heat of vaporization and $h_{\mathrm{liquid}}$, $h_{\mathrm{vapor}}$ are the true molar enthalpies of the liquid and vapor simulation boxes, respectively. True molar enthalpy ($h_x$) is defined as[66]

$$h_x = \frac{H_x}{\sum_i n_{i,x}} \quad (11)$$

where $H_x$ is the total enthalpy in phase $x$ (liquid or vapor) and $n_{i,x}$ is the number of moles of component $i$ (NO or $(NO)_2$) in phase $x$. For the calculation of the molar heat of vaporization, the internal energies and volumes were obtained from RGE calculations and the saturated pressures were obtained from a series of NPT simulations. The total true molar enthalpy is taken as the sum of $h_{\mathrm{liquid}}$ and $h_{\mathrm{gas}}$.

For all simulations in the RGE, $10^3$ initialization cycles were performed followed by an equilibration of $8 \times 10^6$ cycles. This was followed by 5 independent production runs of $3 \times 10^6$ cycles, each. Note that one cycle refers to $N$ number of trial moves, where $N$ is the total number of molecules present in the system. The error bars are computed from the standard deviation of 5 independent production runs. The initial system size for the simulations in the RGE was a total of 400 molecules for temperatures below 140 K and 500 molecules for temperatures above 140 K. The trial moves were selected with the following probabilities: thermalization moves (which includes both translations and rotations) (69%), particle exchanges (15%), volume moves (1%) and reaction moves (15%). For the GE simulations, $10^3$ initialization cycles were performed followed by an equilibration of $8 \times 10^6$ cycles and a production run of $8 \times 10^6$ cycles. The error bars for the GE simulations are computed from the standard deviation of 5 blocks into which the production run was divided. The trial moves were selected with the following probabilities: thermalization moves (84%), particle exchanges (15%) and volume moves (1%). Periodic boundary conditions were considered in all directions for both the RGE and the GE.

## 3 Force field

The structures of NO and $(NO)_2$ were considered rigid according to the corresponding experimental geometries[1,2] (see Fig. 1). We considered two terms in the total potential energy function ($E_{total}$), electrostatic interactions ($E_{electrostatic}$) and van der Waals interactions ($E_{vdW}$),

$$E_{total} = E_{electrostatic} + E_{vdW}. \quad (12)$$

For the electrostatic interactions, the coulombic potential energy function is considered

$$E_{electrostatic} = \frac{1}{4\pi\varepsilon_0}\frac{q_i q_j}{r_{ij}}, \quad (13)$$

where $q$ represents the atomic partial charges, $r_{ij}$ is the distance separating the charges, and $\varepsilon_0$ is the permittivity of vacuum. The atomic partial charges of NO were obtained from the ratio between the experimental dipole moment[67] and the experimental bond length of NO.[1] The partial charges on the atoms of $(NO)_2$ were taken to be the same as that of NO. For the van der Waals interactions, the 12-6 Lennard-Jones (L-J) potential energy function is considered

$$E_{vdW} = 4\varepsilon_{ij}\left[\left(\frac{\sigma_{ij}}{r_{ij}}\right)^{12} - \left(\frac{\sigma_{ij}}{r_{ij}}\right)^{6}\right], \quad (14)$$

where $\sigma$ represents the distance at which the particle–particle interaction energy is zero, and $\varepsilon$ represents the depth of the potential well. The Lorentz–Berthelot[68] mixing rules were used for the L-J parameters of two dissimilar non-bonded atoms,

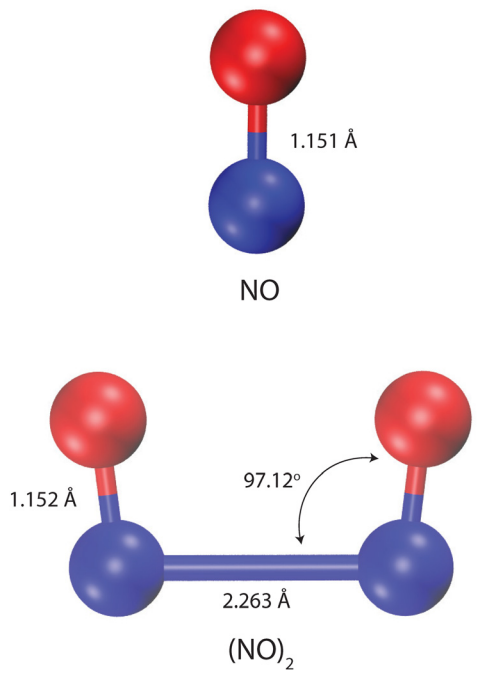


Fig. 1 Experimental values for bond distances and angles of NO and its dimer, $(NO)_2$.[1,2] The blue and red spheres represent N and O atoms, respectively. The visualization is created using the Visual Molecular Dynamics (VMD) software.[3]

Table 1 Our new force field parameters for NO and $(NO)_2$ molecules which are referred to as New FF in the text

| Atoms | $\varepsilon/k_B$/[K] | $\sigma$/[Å] | $q$/[$e$] |
|---|---|---|---|
| | | NO | |
| N | 48.50 | 3.09 | 0.0288 |
| O | 56.29 | 2.94 | −0.0288 |
| | | $(NO)_2$ | |
| N | 47.00 | 3.02 | 0.0288 |
| O | 54.52 | 2.87 | −0.0288 |

$\sigma_{ij} = \frac{\sigma_i + \sigma_j}{2}$, $\varepsilon_{ij} = \sqrt{\varepsilon_i \varepsilon_j}$. A cut-off radius of 10 Å was used for both the Lennard-Jones and Coulombic interactions. The Ewald summation method[69,70] was used to treat long-range Coulombic interactions. The energies and pressures of the simulations were corrected with long-range tail corrections for the L-J interactions.[65] After numerous trials of varying the $\sigma$ and $\varepsilon$ parameters (110 combinations were tested in total), we arrived at the values provided in Table 1. These parameters are referred to as the New FF in the rest of the manuscript. A detailed discussion on the sensitivity analysis of the New FF parameters is provided in Section 5.3.

Lachet *et al.*[36] treat NO as a single L-J sphere with the 12-6 potential function. To model $(NO)_2$, two NO L-J sites separated by a distance of 2.237 Å were used. The individual L-J parameters for each NO site in the dimer are considered to be the same as those for the monomer. The L-J parameters of the force field developed by Lachet *et al.*[36] are listed in Table S9 of the ESI.† Lachet *et al.*[36] neglect electrostatic interactions in their models of NO and $(NO)_2$. The cut-off for the L-J potential was taken as half the length of the simulation box, and interactions beyond the cut-off distance were considered using the long-range tail correction.[65] The force fields for NO and $(NO)_2$ developed by Lachet *et al.*[36] are referred to as Lachet FF in the rest of the manuscript.

In the work by Zhou *et al.*,[38] NO is modeled as a two-site rigid body with partial charges and 12-6 L-J potential on both sites. In their model, the N and O atoms of NO are separated by a distance of 1.15 Å. The Lorentz–Berthelot mixing rules[68] were used for the L-J parameters of two dissimilar nonbonded atoms. The L-J parameters and partial charges taken from the work by Zhou *et al.*[38] are listed in Table S9 of the ESI,† and are referred to as Zhou FF in the rest of the manuscript. Zhou *et al.*[38] do not parameterize a force field for $(NO)_2$.

## 4 Isolated molecular partition functions

As explained in Section 2, to calculate the chemical potential of a component in a reaction, the isolated molecular partition function, $q_{total}(V, T)$, of that component is needed (see eqn (6)). We calculated the isolated molecular partition functions of NO and $(NO)_2$ according to[52]

$$q_{total}(V, T) = q_{trans}(V, T)q_{vib}(T)q_{rot}(T)q_{elec}(T). \quad (15)$$

The translational partition function, $q_{trans}$, is given by[52]

$$q_{trans}(V,T) = \frac{V}{\Lambda^3}, \quad (16)$$

wherein $\Lambda$ is the thermal de Broglie wavelength of the molecule, $\Lambda = \frac{h}{\sqrt{2\pi M k_B T}}$. Here, $h$ is the Planck constant, $M$ is the sum of the masses of all atoms in the molecule, $T$ is the temperature, and $V$ is the volume. In Brick-CFCMC, a reference state of $V = V_0 = 1$ Å$^3$ is used for $q_{trans}$.[52,71]

The vibrational partition function, $q_{vib}$, considering the vibrational ground state energy as the zero of the vibrational energy, is calculated using[52]

$$q_{vib}(T) = \prod_{i=1}^{\alpha} \frac{1}{1 - \exp\left[\frac{-\Theta_{vib,i}}{T}\right]}, \quad (17)$$

in which $i$ runs from 1 to $\alpha$, where $\alpha$ is the number of vibrational degrees of freedom. For a linear molecule, $\alpha = 3n - 5$ and for a non-linear molecule, $\alpha = 3n - 6$, where $n$ is the number of atoms in the molecule. $\Theta_{vib,i} = \frac{h\nu_i}{k_B}$ is the characteristic vibrational temperature corresponding to the $i$th normal mode with vibrational frequency, $\nu_i$.

The energy levels ($\varepsilon_J$) of a diatomic molecule such as NO, under the rigid-rotor approximation is given by[52]

$$\varepsilon_J = \frac{h^2 J(J+1)}{8\pi^2 I}, \quad (18)$$

where $J$ is the rotational quantum number, $I$ is the principal moment of inertia. The energy level corresponding to $J = 0$ is chosen as the zero of the rotational energy for the calculation of the rotational partition function, $q_{rot}$. The rotational constant of an axis, $X$, is related to the moment of inertia of that axis, $I$, by $I = \frac{h}{8\pi^2 X}$. For a diatomic molecule such as NO, $q_{rot}$ is given by[52]

$$q_{rot}(T) = \frac{T}{\sigma_{rot}\Theta_{rot}}, \quad (19)$$

where $\Theta_{rot} = \frac{h^2}{8\pi^2 I k_B}$ is the characteristic rotational temperature. $\sigma_{rot}$ is the rotational symmetry number of the molecule, which is the number of indistinguishable configurations the molecule can be brought into by rotation about its centre of mass.[72] For NO, $\sigma_{rot} = 1$. The rotational partition function, $q_{rot}$, for $(NO)_2$, which is a non-linear polyatomic species, is calculated using[52]

$$q_{rot}(T) = \frac{\sqrt{\pi}}{\sigma_{rot}}\left(\frac{T^3}{\Theta_{rot,A}\Theta_{rot,B}\Theta_{rot,C}}\right)^{1/2}, \quad (20)$$

where, $\sigma_{rot,(NO)_2}$ is the rotational symmetry number of $(NO)_2$ and is equal to 1, $\Theta_{rot,A}$, $\Theta_{rot,B}$ and $\Theta_{rot,C}$ are the characteristic rotational temperatures corresponding to the principal moments of inertia, $I_A$, $I_B$ and $I_C$, respectively. The rotational[73] and vibrational[2,74,75] partition functions of NO and $(NO)_2$ were calculated using experimental values of rotational and vibrational frequencies (see Tables S2 and S3 of the ESI†).

Finally, the electronic partition function, $q_{elec}$, is calculated using[52]

$$q_{elec}(T) = g_{e1}\exp\left[\frac{D_0}{k_B T}\right] \quad (21)$$

where $g_{e1}$ is the degeneracy of the electronic ground state. $g_{e1,NO} = 2$[76] and $g_{e1,(NO)_2} = 1$.[77] $D_0$ is the atomization energy of the molecule which is defined as the difference between the enthalpy of formation of the molecule and the sum of the enthalpies of formation of the dissociated atoms which constituted the molecule.[52] The energy of the infinitely dissociated atoms at the ground electronic state is taken as the zero of the electronic energy.

The value of $D_0$ for NO was calculated from the enthalpies of formation of NO, N and O, which were obtained from the JANAF tables;[78] $D_{0,NO}$ = 629.82 kJ mol$^{-1}$. The atomization energy of $(NO)_2$, $D_{0,(NO)_2}$, was not readily available in the JANAF tables,[78] but can be calculated by

$$D_{0,(NO)_2} = 2D_{0,NO} + BDE_{(NO)_2}, \quad (22)$$

where $BDE_{(NO)_2}$ is the bond dissociation energy of $(NO)_2$, which is the energy required to break the N–N bond of $(NO)_2$.

The values of $BDE_{(NO)_2}$ reported in literature, depending on the accuracy of the theoretical method or experimental technique used, are in the range of 7.64 to 13.8 kJ mol$^{-1}$.[2,33,39,79–83] Due to the large variations in the values of $BDE_{(NO)_2}$ reported in literature, an approach used by Turner *et al.*[83] and Johnson *et al.*[39] was to adjust the value of $BDE_{(NO)_2}$ to reproduce the experimental dimer mole fraction in the liquid phase. With this approach, Turner *et al.*[83] obtained a value of $BDE_{(NO)_2}$ = 10.9 kJ mol$^{-1}$ and Johnson *et al.*[39] achieved a value of $BDE_{(NO)_2}$ = 13.6 kJ mol$^{-1}$. In our work, we also varied the value of $BDE_{(NO)_2}$ between 7.64 and 13.8 kJ mol$^{-1}$ to predict the mole fractions of dimer in the liquid phase as well as the VLE properties of the reactive NO–$(NO)_2$ system in agreement the available data. After numerous iterations, we obtained a value of $BDE_{(NO)_2}$ = 13.06 kJ mol$^{-1}$ which corresponds to a value of $D_{0,(NO)_2}$ = 1269 kJ mol$^{-1}$.

The isolated molecular partition functions of NO and $(NO)_2$ were calculated according to eqn (15) for temperatures ranging from 121.5 K to 165 K. A correlation was fitted to the respective isolated molecular partition functions, which is given by

$$\ln\left[\frac{qV_0}{\Lambda^3}\right]_{NO} = \frac{75\,396.84}{T} + 11.26, \quad (23)$$

$$\ln\left[\frac{qV_0}{\Lambda^3}\right]_{(NO)_2} = \frac{152\,020.74}{T} + 19.42, \quad (24)$$

where $q$ is the isolated molecule partition function excluding the translational contribution.

# 5 Results and discussion

The validation of the New FF with the experimental VLE properties of the reactive NO–$(NO)_2$ system is discussed in Section 5.1. The performance of the New FF compared to the Lachet FF and Zhou FF in predicting the VLE properties of pure NO and pure $(NO)_2$ are discussed in Section 5.2. Finally, the dependence of the VLE of the reactive NO–$(NO)_2$ system on the $D_{0,(NO)_2}$ and L-J parameters ($\sigma$ and $\varepsilon$) is investigated in Section 5.3.

## 5.1 Reactive NO–$(NO)_2$ systems

**5.1.1 Coexistence densities.** The coexistence densities of the liquid and vapor phases were computed at ten different temperatures ranging from 121.5 K to 165 K using the New FF and the Lachet FF. The results are presented in Fig. 2 along with the available experimental data.[84] The raw data are available in Table S5 of the ESI.† The average absolute deviation between the liquid densities calculated using the New FF and the experimental liquid densities is 2.32 kg $m^{-3}$ (0.2%). Our results using the Lachet FF are also in agreement with those presented in the original paper by Lachet *et al.*[36] The Lachet FF overestimates the liquid densities at lower temperatures (120 K to 140 K) and underestimates the liquid densities at higher temperatures (>140 K). The average absolute deviation between the liquid densities calculated using the Lachet FF and the experimental liquid densities is 36.89 kg $m^{-3}$ (3.3%) which is much larger than that calculated using the New FF.

The predicted critical temperature ($T_c$), density ($\rho_c$), and pressure ($P_c$) using the New FF and Lachet FF are presented in Table 2 along with experimental data.[84] The predicted critical density using the New FF is 489.59 kg $m^{-3}$ which is within 27.76 kg $m^{-3}$ (5.4%) of the experimental value. The critical temperature predicted using the New FF is 182.51 K which has a deviation of 1.3% from the experimental critical temperature. The critical density and temperature predicted by the Lachet FF deviate from the experimental values by 9.8% and 3.4%, respectively.

Table 2 Critical temperatures ($T_c$), densities ($\rho_c$), and pressures ($P_c$) calculated using the New FF and the Lachet FF.[36] Errors (written as subscripts) are estimated using standard deviations of 5 independent simulations. Experimental values[84] are added for comparison

| | $T_c$/[K] | $\rho_c$/[kg $m^{-3}$] | $P_c$/[MPa] |
|---|---|---|---|
| New FF | $182.51_{0.54}$ | $489.59_{1.52}$ | $6.24_{0.15}$ |
| Lachet FF[36] | 174.03 | 466.60 | 6.37 |
| Experimental[84] | 180.15 | 517.35 | 6.48 |

**5.1.2 Dimer mole fractions.** The mole fraction of $(NO)_2$ in the liquid phase of the NO–$(NO)_2$ system obtained using the New FF and the Lachet FF is presented in Fig. 3. The raw data are presented in Table S6 of the ESI.† The experimental values, in the temperature range from 110 K to 120 K, are taken from the work of Smith and Johnston.[31] Walsh *et al.*[30] used a modified Wertheim's association theory and Kohler[29] used the theory of corresponding states of mixture to theoretically estimate the dimer mole fractions in the liquid phase. The data from both works are presented in Fig. 3 for comparison.

At 110 K, the predicted $(NO)_2$ mole fraction using the New FF is 0.92, while the corresponding experimental value is 0.95. The mole fraction of dimers predicted using the New FF monotonically decreases with increasing temperature. $(NO)_2$ mole fraction obtained using the New FF is in better agreement with the estimate values of Walsh *et al.*[30] for the temperature range (121.5 K to 165 K). The dimer mole fractions predicted using the Lachet FF is in better agreement with the estimates by Kohler.[29] We note that our calculations using the Lachet FF are

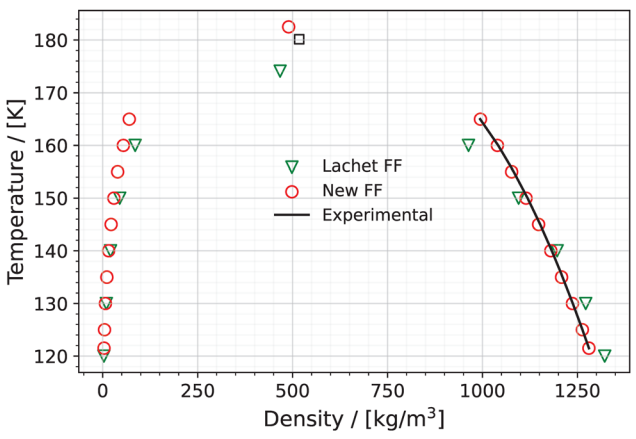


Fig. 2 Vapor–liquid coexistence densities of the NO–$(NO)_2$ system predicted using the New FF as a function of temperature (red circles). Error bars for the New FF are estimated based on the standard deviation of 5 independent simulations and are much smaller than the symbols used in the figure. The orthobaric densities obtained using the Lachet FF[36] (green triangles) along with the experimental liquid densities[84] (black line) are added for comparison. The experimental critical point (black square) is also shown in the figure.

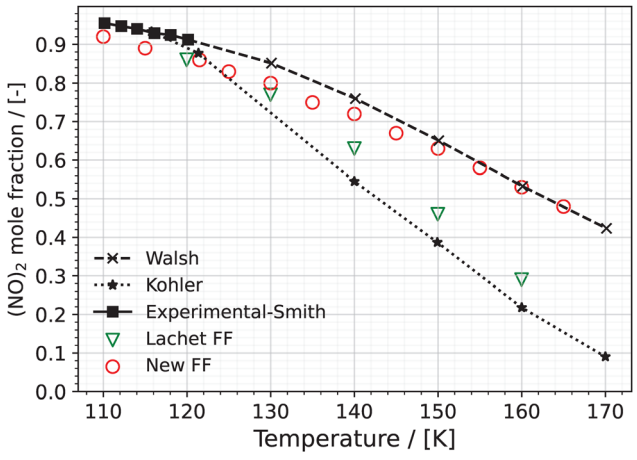


Fig. 3 Dimer mole fractions in the NO–$(NO)_2$ liquid phase, which is at coexistence with the vapor phase, predicted using the New FF (red circles) as well as the Lachet FF[36] (green triangles) as a function of temperature. Error bars for the New FF are estimated based on the standard deviation of 5 independent simulations and are much smaller than the symbols used in the figure. The experimental mole fractions (black squares) from 110 K to 120 K[31] and extrapolated estimates of Walsh *et al.*[30] and Kohler[29] from 120 K to 170 K are added for comparison.

 

in agreement with those presented in the original work by Lachet *et al.*[36] In the vapor phase, monomers have a more dominant presence for the temperature range 121.5 K to 165 K. The presence of dimers increases as the temperature increases, although slightly (see Table S6 of the ESI†). At 121.5 K, the New FF predicts a dimer mole fraction of 6%, whereas the Lachet FF predicts a dimer mole fraction of 0.4%. One reason for the lower mole fraction of $(NO)_2$ predicted in the work of Lachet *et al.*[36] compared to our work using the New FF could be attributed to the differences between the standard chemical potential, $\mu^0$ (defined as $\mu^0 = -k_B T \ln\left[\frac{qV_0}{\Lambda^3}\right]$[42,62]) of $(NO)_2$ and 2NO. The differences between the standard chemical potential of $(NO)_2$ and 2NO used in the work of Lachet *et al.* favor more NO molecules in the system.[36,85]

**5.1.3 Coexistence pressures.** In Fig. 4, the inverse temperature dependence of the coexistence pressures of the NO–$(NO)_2$ system predicted using the New FF and the Lachet FF are presented on a logarithmic scale. The experimental values are also added for comparison. The average absolute deviations between the computed vapor pressures using the New FF and the experimental vapor pressures is 15%. The corresponding value for Lachet FF is 17%. Higher values of vapor pressures predicted using the Lachet FF compared to the New FF could be traced back to the different isolated molecular partition functions used in Lachet *et al.*[36] compared to our work; or alternatively the differences between the standard chemical potential $\left(\mu^0 = -k_B T \ln\left[\frac{qV_0}{\Lambda^3}\right]\right)$ of $(NO)_2$ and 2NO used in Lachet *et al.*[36] compared to our work, which leads to differences in compositions. The isolated molecular partition functions in the work of Lachet *et al.*[36] favor more NO molecules in both the vapor and liquid simulation boxes compared to our systems. This leads to higher vapor pressures for Lachet *et al.*[36] The critical pressure is obtained by extrapolating the vapor pressure curve to the critical temperature using eqn (9). The critical pressure using the New FF is 6.24 MPa (3.9% deviation from the experimental critical pressure) and that predicted using the Lachet FF is 6.37 MPa (1.7% deviation from the experimental value). See Table 2.

**5.1.4 Heats of vaporization.** The temperature dependence of the heats of vaporization for the system containing NO and its dimer predicted using the New FF and the Lachet FF is shown in Fig. 5 (see eqn (10)). The experimental values are also shown for comparison. The results using the New FF are in good agreement with the experimental vaporization enthalpies. The average absolute deviation between the experimental enthalpies of vaporization and those predicted by the New FF is 0.46 kJ $mol^{-1}$ (4.4%). This value for the Lachet FF is 0.82 kJ $mol^{-1}$ (8%). The Lachet force field overestimates the heats of vaporization at lower temperatures (120 K and 130 K) and underestimates at higher temperatures (150 K and 160 K). At 140 K the Lachet FF is in good agreement with the experimental value.

### 5.2 Non-reactive pure NO and pure $(NO)_2$ systems

**5.2.1 Properties of pure NO.** The coexistence densities of pure (unreactive) NO computed using the New FF, the Lachet FF, and the force field developed by Zhou *et al.*[38] (Zhou FF), as a function of temperature, are shown in Fig. 6. The saturated vapor pressures of pure NO for temperatures between 120 K and 160 K computed using these three force fields are shown in Fig. 7. The predicted critical densities, temperatures and pressures of pure NO are shown in Table S10 of the ESI.† The vapor phase densities of pure NO using the Lachet FF are in excellent agreement with the vapor phase densities computed using the New FF. The liquid densities of NO using the New FF are higher than those computed using the Lachet FF for the entire temperature range of 120 K to 160 K. The differences between

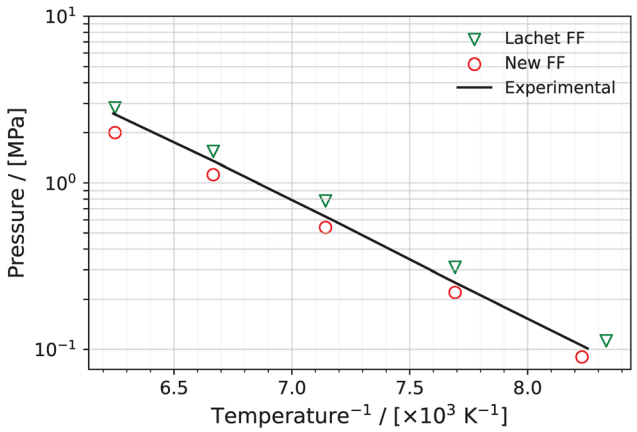


Fig. 4 Inverse temperature dependence of the coexistence pressures of the NO–$(NO)_2$ system predicted using the New FF (red circles) and the Lachet FF[36] (green triangles), in logarithmic scale. Error bars for the New FF are computed based on the standard deviation and are smaller than the symbols used in the figure. Experimental data[84] for the coexistence pressures is represented by the black line.

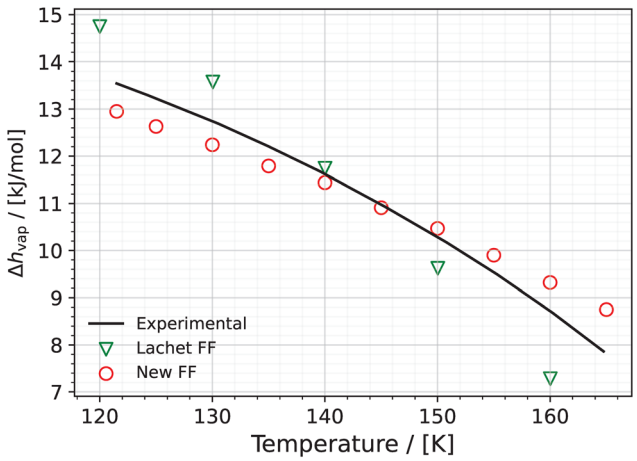


Fig. 5 Heat of vaporization *versus* temperature for the reactive NO–$(NO)_2$ system obtained using the New FF (red circles) and the Lachet FF[36] (green triangles). Error bars for the New FF are computed based on the standard deviation of 5 independent simulations and are much smaller than the symbols used in the figure. Experimental values[84] (black line) are added for comparison.

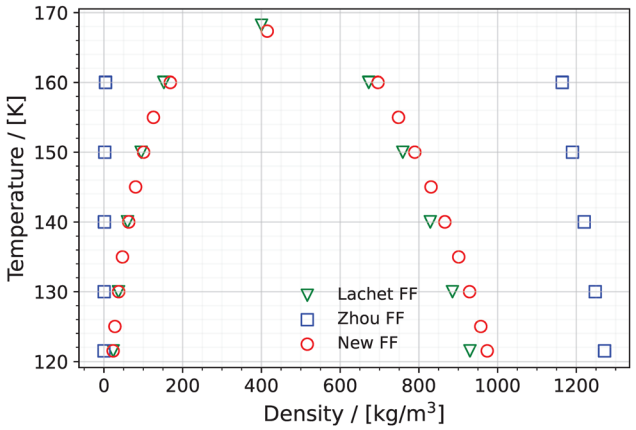


Fig. 6 Coexisting vapor and liquid densities of pure (unreactive) NO using the New FF (red circles), the Zhou FF[38] (blue squares) and the Lachet FF[36] (green triangles). Error bars are estimated based on the standard deviation of 5 blocks into which the production run was divided and are much smaller than the symbols used in the figure. The critical points of both the New FF and Lachet FF are indicated in the figure. The critical points of the Zhou FF is not shown in the figure, but it is listed in Table S9 (ESI†).

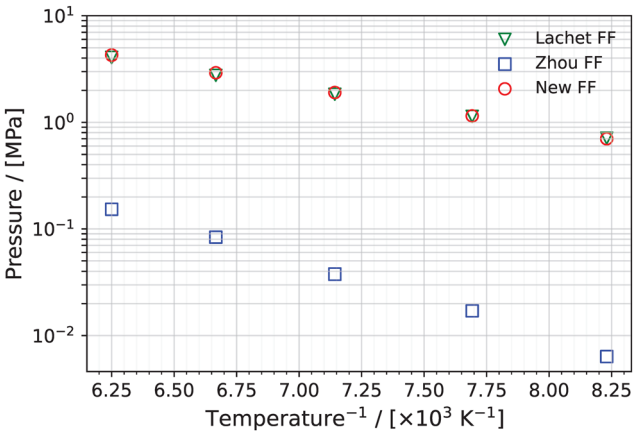


Fig. 7 Inverse temperature dependence of the saturated vapor pressures of pure NO using the New FF (red circles), the Zhou FF[38] (blue squares) and the Lachet FF[36] (green triangles), on logarithmic scale. Error bars for the New FF are computed based on the standard deviation and are smaller than the symbols used in the figure.

the liquid densities of NO calculated using the Lachet FF and the New FF are reduced as the temperature reaches the critical temperature (168.20 K for Lachet FF and 167.34 K for the New FF). The vapor densities computed using the Zhou FF are much lower (on average 99%) than those calculated using the Lachet FF and the New FF, while the liquid densities predicted using the Zhou FF are much higher (on average 48%) than the densities of the other two force fields. This is because the Zhou FF was optimized to reproduce the experimental density of liquid NO–$(NO)_2$ without taking the presence of dimer $(NO)_2$ into account. The values of the L-J energy parameter $\varepsilon$ of N and O in the Zhou FF are also higher (by 68%) than the New FF (see Table S8 of the ESI†) which leads to lower vapor phase densities, as higher $\varepsilon$ contributes to higher intermolecular interactions in the liquid, making it difficult for molecules to move to the vapor phase. This is evident in Fig. 7, where the saturated vapor pressures ($P_{sat}$) of the Zhou FF are lower, showing a difference of *ca.* 4 MPa at 160 K, compared to the New FF and the Lachet FF. The critical saturated vapor pressure ($P_c$) of the Zhou FF is larger than that of the New FF and Lachet FF as the critical temperature ($T_c$) of the Zhou FF is higher compared to the other two force fields. The New FF and the Lachet FF have comparable values of $P_{sat}$ as their vapor phase densities have similar values (see Fig. 6). The values of $P_c$ of the New FF and the Lachet FF differ only by 0.18 MPa.

**5.2.2 Properties of pure $(NO)_2$.** Fig. 8 shows the vapor and liquid densities of pure (unreactive) $(NO)_2$ as a function of temperature computed using the Lachet FF and the New FF. The saturated vapor pressures of pure $(NO)_2$ as a function of the temperature computed using the New FF and Lachet FF are shown in Fig. 9. Note that the results for the Zhou FF is not included as there are no force field parameters for $(NO)_2$ in the original work of Zhou *et al.*[38]

The predicted critical temperatures, densities, and pressures are listed in Table S9 of the ESI.† The predicted critical temperature, $T_c$, using the New FF is 243.78 K which is smaller than the predicted critical temperature using the Lachet FF (298.37 K). The critical densities ($\rho_c$) predicted by the two force fields are in agreement (454.28 kg m$^{-3}$ for the New FF and 449.95 kg m$^{-3}$ for the Lachet FF).

The saturated vapor pressures calculated using the Lachet FF and the New FF are shown in Fig. 9. $P_{sat}$ values computed using the Lachet FF are smaller (on average by 77.2%) than the $P_{sat}$ values computed using the New FF in the temperature range of 125 K to 225 K. However, the $P_c$ computed using the Lachet FF is larger than the $P_c$ calculated using the New FF by 0.8 MPa. This is attributed to the larger $T_c$ predicted by the Lachet FF compared to the $T_c$ predicted by the New FF (see Table S10 of the ESI†).

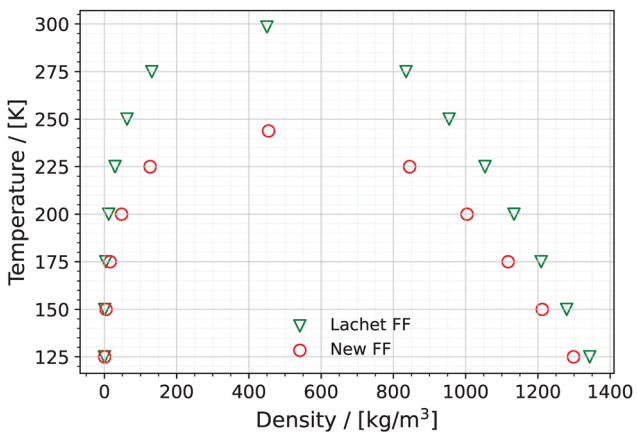


Fig. 8 Coexisting vapor and liquid densities of pure $(NO)_2$ using the New FF (red circles) and the Lachet FF[36] (green triangles). Error bars are estimated based on the standard deviation of 5 blocks into which the production run was divided and are much smaller than the symbols used in the figure. The critical points are also shown in the figure.

 

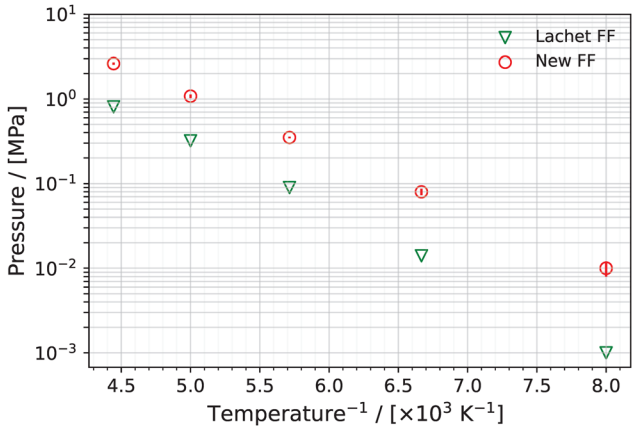


Fig. 9 Inverse temperature dependence of the saturated vapor pressures of pure $(NO)_2$ using the New FF (red circles) and the Lachet FF[36] (green triangles), on logarithmic scale. Error bars for the New FF are computed based on the standard deviation.

### 5.3 Sensitivity analysis

The VLE properties of the reactive NO–$(NO)_2$ system are sensitive to the atomization energy of $(NO)_2$ ($D_{0,(NO)_2}$) and the L-J parameters, $\sigma$ and $\varepsilon$ of NO and $(NO)_2$. We performed a series of simulations to systematically analyze the dependence of the VLE properties of the reactive NO–$(NO)_2$ system on $D_{0,(NO)_2}$ and L-J parameters, and hence reflect upon the uniqueness of our new force field parameters. These simulations and their main results are discussed below.

**5.3.1 Effect of $D_{0,(NO)_2}$ on VLE properties of reactive NO–$(NO)_2$ system.** In the first series of simulations, we considered three values for $D_{0,(NO)_2}$ which correspond to three values of $BDE_{(NO)_2}$ that are within the range of the reported experimental and theoretical values for $BDE_{(NO)_2}$ in the literature (7.64–13.8 kJ mol$^{-1}$).[2,32,75,79–82,86] These values are listed in Table S10 of the ESI.† $D_{0,(NO)_2}$ = 1269 kJ mol$^{-1}$ is the value with which the VLE properties could be computed in agreement with experiments (see Section 5.1). In these simulations, the L-J parameters and the partial charges are fixed as in Table 1. These simulations are performed in the reactive Gibbs ensemble.

The vapor–liquid coexistence densities and $(NO)_2$ mole fractions in the liquid phase of the reactive NO–$(NO)_2$ system for these four values of $D_{0,(NO)_2}$ are shown in Fig. S2 and S3 of the ESI,† respectively. Even though the values of $D_{0,(NO)_2}$ are only different by 4 kJ mol$^{-1}$ (difference between the highest and lowest value in the set), the differences in the corresponding dimer mole fractions in the liquid phase is significant (56% difference in the mole fractions at 160 K between the systems with the highest and lowest value of $D_{0,(NO)_2}$). Moreover, higher values of $D_{0,(NO)_2}$ tend to have more negative slopes for the liquid densities (see Fig. S2 of the ESI†). This could be attributed to the presence of more dimer species in the liquid phase. This results in a higher critical temperature compared to the systems with lower values of $D_{0,(NO)_2}$ (see Table S11 of the ESI†).

**5.3.2 Effect of L-J parameters on VLE properties of reactive NO–$(NO)_2$ system.** In a second series of simulations, the values of $D_{0,(NO)_2}$ = 1269 kJ mol$^{-1}$ and partial charges (see Table 1) are fixed, while twelve different combinations of L-J parameters are considered. In each combination, the L-J parameters ($\sigma$ or $\varepsilon$) of NO and/or $(NO)_2$ are varied by ±10% compared to the respective parameters of the New FF. These parameters are labeled FF-a to FF-l: $\sigma_{(NO)_2}$ in FF-a (b), $\varepsilon_{(NO)_2}$ in FF-c (d), $\sigma_{NO}$ in FF-e (f), $\varepsilon_{NO}$ in FF-g (h), $\sigma_{NO}$ and $\sigma_{(NO)_2}$ in FF-i (j), and $\varepsilon_{NO}$ and $\varepsilon_{(NO)_2}$ in FF-k (l), are varied by −10% (10%). These parameters are shown in Table S12 of the ESI.† These simulations are also performed in the reactive Gibbs ensemble.

The coexistence densities, dimer mole fractions in the liquid phase, coexistence pressures, heats of vaporization, and total enthalpies of the reactive NO–$(NO)_2$ system were computed using FF-a to FF-l and are shown in Fig. S4–S33 of the ESI.†

An increase in the L-J parameters of $(NO)_2$, $\sigma_{(NO)_2}$ (FF-b) or $\varepsilon_{(NO)_2}$ (FF-d), or NO, $\sigma_{NO}$ (FF-f) or $\varepsilon_{NO}$ (FF-h), results in an increase in the mole fraction of that species, $(NO)_2$ (see Fig. S5 and S10 of the ESI†) or NO (see Fig. S15 and S20 of the ESI†), in the liquid phase of the system. Increasing the values of the L-J parameters of a species makes it energetically favorable to increase the concentration of that species in the system. This can be seen by comparing two simple L-J systems that differ in the values of the L-J parameters, as shown in Fig. S34 of the ESI† (two systems with the same value of $\sigma$ but different values of $\varepsilon$) and Fig. S35 of the ESI† (two systems with the same value of $\varepsilon$ but different values of $\sigma$). With an increase in $\sigma$ or $\varepsilon$, the area of the attractive potential L-J increases. Therefore, with the increase in the values of the L-J parameters ($\sigma$ or $\varepsilon$) of NO or $(NO)_2$, it becomes energetically favorable to increase the concentration of NO or $(NO)_2$ in the NO–$(NO)_2$ system.

The increase in the mole fraction of $(NO)_2$ or NO affects the VLE properties of the reactive system, including the total enthalpies of the system. An increase in the dimer mole fraction lowers the total enthalpy of the system; see Fig. S8, S13, S18 and S23 of the ESI.† This is supported by the exothermic nature of dimer formation, which causes heat dissipation, and thereby, reduction of the total enthalpy of the system. However, an increase in monomer concentrations increases the total enthalpy of the system. This scenario may be supported by the endothermic nature of N–N bond dissociation between two NO entities in ($(NO)_2$), which leads to an increase in the total enthalpy of the system. The dimer mole fractions in the liquid phase when the L-J parameters of NO and $(NO)_2$ ($\sigma$ in FF-i (j) and $\varepsilon$ in FF-k (l)) are simultaneously varied by ±10% compared to the New FF, follow a similar trend as when only the L-J parameters of $(NO)_2$ is varied ($\sigma_{(NO)_2}$ in FF-a (b) and $\varepsilon_{(NO)_2}$ in FF-c (d)); see Fig. S25 and S30 of the ESI.† This could be because the liquid phase is predominantly composed of dimers.

Although we demonstrated that the VLE properties of the reactive NO–$(NO)_2$ system depends on both $D_{0,(NO)_2}$ (or subsequently $BDE_{(NO)_2}$) and the L-J parameters of NO and $(NO)_2$ species, this may not be the case for all the reactive systems. An example is a reactive $NO_2$–$N_2O_4$ system. The VLE properties of reactive $NO_2$–$N_2O_4$ are almost exclusively affected by the values of $BDE_{N_2O_4}$ and not by the values of L-J parameter as can be inferred by the work of Polat *et al.*[62] As explained by Johnson *et al.*,[39] the values of BDE determine the association strength of a

fluid. A fluid is weakly (strongly) associating if the value of BDE is small (large).[39] The concluded value of BDE for $(NO)_2$ in our study is 13.06 kJ mol$^{-1}$ (*i.e.*, $D_{0,(NO)_2}$ = 1269 kJ mol$^{-1}$), which is much smaller than value of BDE for $N_2O_4$ ($\sim$50 kJ mol$^{-1}$).[61] Accordingly, $NO_2$–$N_2O_4$ fluid is a more strongly associating fluid than NO–$(NO)_2$ fluid. Therefore, the dependence of the VLE properties of a reactive fluid on the values of L-J parameters may be determined by the association strength of that fluid.

## 6 Conclusions

Our force field is capable of predicting the VLE properties of the reactive NO–$(NO)_2$ system (*i.e.*, coexistence vapor–liquid densities, dimer mole fractions in liquid phase, saturated vapor pressures, and heats of vaporization) in excellent agreement with experimental values for the temperature range 120 K to 170 K. For pure NO, the predicted VLE properties using our force field parameters agree well with those using the Lachet FF. However, there are large deviations between the predictions using the Zhou FF and predictions using our force field parameters or the Lachet FF. The Zhou FF was developed to reproduce the experimental density and heat of vaporization of NO at its boiling point without considering the formation of a dimer at this temperature. This may be the reason for the large deviations of the VLE properties of pure NO predicted by the Zhou FF from those predicted by the New FF and Lachet FF. For pure $(NO)_2$, the liquid densities using the Lachet FF are larger (on average, by 11%) than the predictions using our force field parameters. The Lachet FF predicts smaller saturated vapor pressures (on average *ca.* 80%) compared to our force field. We also performed a systematic parameter study to analyze the impact of individual L-J parameters ($\sigma$ and $\varepsilon$ of NO and $(NO)_2$) as well as the atomization energy of $(NO)_2$, $D_{0,(NO)_2}$, or alternatively the bond dissociation energy of $(NO)_2$, $BDE_{(NO)_2}$, on the VLE properties of the reactive NO–$(NO)_2$ system. Our results show that the VLE properties of the reactive NO–$(NO)_2$ system are affected by both the L-J parameters and the atomization energy of the NO dimer. This is in contrast to a previously studied reactive $NO_2$–$N_2O_4$ system where the VLE properties are mainly affected by the atomization energy of $NO_2$ dimer. This can be attributed to the association strength of reactive fluids. A fluid is weakly (strongly) associating if the value of BDE is small (large). The concluded value of the BDE for $(NO)_2$ in our study is 13.06 kJ mol$^{-1}$, which is much smaller than the BDE of $N_2O_4$ ($\sim$50 kJ mol$^{-1}$). Accordingly, the $NO_2$–$N_2O_4$ fluid is a more strongly associating fluid than the NO–$(NO)_2$ fluid. Therefore, the VLE properties of reactive NO–$(NO)_2$ system are affected by both L-J parameters and the atomization energy of the dimer, while the VLE properties of reactive $NO_2$–$N_2O_4$ are only affected by the atomization energy of the dimer.

## Author contributions

All authors conceived the work. TS carried out the simulations and data analysis. All authors provided critical feedback on the interpretation of data analysis. BB supervised the project. TS and BB wrote the manuscript in collaboration with TV and SC.

## Data availability

The data supporting this manuscript have been included as part of the ESI.† The input files to run Brick-CFCMC simulations as well as the output files are provided at **https://doi.org/10.5281/zenodo.15524759**.

## Conflicts of interest

There are no conflicts to declare.

## Acknowledgements

TS thanks the Institute for Complex Molecular Systems for financial support.

## References

1 E. F. Horn and F. P. Dickey, *J. Chem. Phys.*, 1964, **41**, 1614–1620.
2 A. R. McKellar, J. Watson and B. Howard, *Mol. Phys.*, 1995, **86**, 273–286.
3 W. Humphrey, A. Dalke and K. Schulten, *J. Mol. Graphics*, 1996, **14**, 33–38.
4 P. Lukes, E. Dolezalova, I. Sisrova and M. Clupek, *Plasma Sources Sci. Technol.*, 2014, **23**, 015019.
5 M. A. Malik, *Plasma Chem. Plasma Process.*, 2016, **36**, 737–766.
6 Z. Machala, B. Tarabová, D. Sersenová, M. Janda and K. Hensel, *J. Phys. D: Appl. Phys.*, 2018, **52**, 034002.
7 K. Tachibana and T. Nakamura, *J. Phys. D: Appl. Phys.*, 2019, **52**, 385202.
8 D. B. Graves, *J. Phys. D: Appl. Phys.*, 2012, **45**, 263001.
9 X. Lu, G. V. Naidis, M. Laroussi, S. Reuter, D. B. Graves and K. Ostrikov, *Phys. Rep.*, 2016, **630**, 1–84.
10 D. B. Graves, *Plasma Processes Polym.*, 2014, **11**, 1120–1127.
11 D. P. Park, K. Davis, S. Gilani, C.-A. Alonzo, D. Dobrynin, G. Friedman, A. Fridman, A. Rabinovich and G. Fridman, *Curr. Appl. Phys.*, 2013, **13**, S19–S29.
12 N. Puač, M. Gherardi and M. Shiratani, *Plasma Processes Polym.*, 2018, **15**, 1700174.
13 P. Ranieri, N. Sponsel, J. Kizer, M. Rojas-Pierce, R. Hernández, L. Gatiboni, A. Grunden and K. Stapelmann, *Plasma Processes Polym.*, 2021, **18**, 2000162.
14 C. V. Suschek and C. Opländer, *Clin. Plasma Med.*, 2016, **4**, 1–8.
15 A. V. Butenko, A. B. Shekhter, A. V. Pekshev, A. B. Vagapov, A. L. Fayzullin, N. B. Serejnikova, N. A. Sharapov, V. A. Zaborova and V. N. Vasilets, *Clin. Plasma Med.*, 2020, **19**, 100112.

 

16 A. Lindsay, B. Byrns, W. King, A. Andhvarapou, J. Fields, D. Knappe, W. Fonteno and S. Shannon, *Plasma Chem. Plasma Process.*, 2014, **34**, 1271–1290.
17 C. Bradu, K. Kutasi, M. Magureanu, N. Puač and S. Živković, *J. Phys. D: Appl. Phys.*, 2020, **53**, 223001.
18 D. Guo, H. Liu, L. Zhou, J. Xie and C. He, *J. Sci. Food Agric.*, 2021, **101**, 4891–4899.
19 W. Tian and M. J. Kushner, *J. Phys. D: Appl. Phys.*, 2014, **47**, 165201.
20 A. M. Lietz and M. J. Kushner, *J. Phys. D: Appl. Phys.*, 2016, **49**, 425204.
21 A. D. Lindsay, D. B. Graves and S. C. Shannon, *J. Phys. D: Appl. Phys.*, 2016, **49**, 235204.
22 C. Verlackt, W. Van Boxem and A. Bogaerts, *Phys. Chem. Chem. Phys.*, 2018, **20**, 6845–6859.
23 K. Ikuse and S. Hamaguchi, *Jpn. J. Appl. Phys.*, 2022, **61**, 076002.
24 P. J. Bruggeman, M. J. Kushner, B. R. Locke, J. G. Gardeniers, W. Graham, D. B. Graves, R. Hofman-Caris, D. Maric, J. P. Reid and E. Ceriani, *et al.*, *Plasma Sources Sci. Technol.*, 2016, **25**, 053002.
25 T. H. G. Saji, J. M. Vicent-Luna, T. J. H. Vlugt, S. Calero and B. Bagheri, *J. Mol. Liq.*, 2024, **401**, 124530.
26 M. N. Hughes, *Methods Enzymol.*, 2008, **436**, 3–19.
27 H. Hoshina, M. Slipchenko, K. Prozument, D. Verma, M. W. Schmidt, J. Ivanic and A. F. Vilesov, *J. Phys. Chem. A*, 2016, **120**, 527–534.
28 S. Marinakis, C. Cockrell, K. Trachenko, T. F. Headen and A. K. Soper, *J. Phys. Chem. B*, 2022, **126**, 9860–9870.
29 F. Kohler, H. J. Guedes, J. Revés and M. N. da Ponte, *J. Mol. Liq.*, 1995, **67**, 105–123.
30 J. M. Walsh, H. J. Guedes and K. E. Gubbins, *J. Phys. Chem.*, 1992, **96**, 10995–11004.
31 A. L. Smith and H. L. Johnston, *J. Am. Chem. Soc.*, 1952, **74**, 4696–4698.
32 J. K. Park and H. Sun, *Chem. Phys.*, 2001, **263**, 61–68.
33 R. Sayós, R. Valero, J. Anglada and M. González, *J. Chem. Phys.*, 2000, **112**, 6608–6624.
34 F. Kohler, M. Bohn, J. Fischer and R. Zimmermann, *Monatsh. Chem.*, 1987, **118**, 169–182.
35 J. O. Hirschfelder, C. F. Curtiss and R. B. Bird, *The molecular theory of gases and liquids*, John Wiley & Sons, 1964.
36 V. Lachet, B. Creton, T. de Bruin, E. Bourasseau, N. Desbiens, Ø. Wilhelmsen and M. Hammer, *Fluid Phase Equilib.*, 2012, **322**, 66–78.
37 J. Yang, Y. Ren, A.-M. Tian and H. Sun, *J. Phys. Chem. B*, 2000, **104**, 4951–4957.
38 Z. Zhou, B. Todd, K. P. Travis and R. J. Sadus, *J. Chem. Phys.*, 2005, **123**, 054505.
39 J. K. Johnson, A. Z. Panagiotopoulos and K. E. Gubbins, *Mol. Phys.*, 1994, **81**, 717–733.
40 J. K. Johnson, *Adv. Chem. Phys.*, 1999, **105**, 461–481.
41 W. Smith and B. Triska, *J. Chem. Phys.*, 1994, **100**, 3019–3027.
42 A. Poursaeidesfahani, R. Hens, A. Rahbari, M. Ramdin, D. Dubbeldam and T. J. H. Vlugt, *J. Chem. Theory Comput.*, 2017, **13**, 4452–4466.
43 C. Heath Turner, J. K. Brennan, M. Lisal, W. R. Smith, J. Karl Johnson and K. E. Gubbins, *Mol. Simul.*, 2008, **34**, 119–146.
44 S. C. Glotzer, D. Stauffer and N. Jan, *Phys. Rev. Lett.*, 1994, **72**, 4109.
45 J. Sterpenich, M.-C. Caumon, V. Lachet, B. Creton, M. El Jarmouni, A. Randi and P. Robert, *J. Raman Spectrosc.*, 2022, **53**, 645–653.
46 B. Creton, C. Nieto-Draghi, T. De Bruin, V. Lachet, E. El Ahmar, A. Valtz, C. Coquelet, S. Lasala, R. Privat and J.-N. Jaubert, *Fluid Phase Equilib.*, 2018, **461**, 84–100.
47 W. Sun, L.-C. Lin, X. Peng and B. Smit, *AIChE J.*, 2014, **60**, 2314–2323.
48 N. Qiu, X. Bai, J. Xu, N. Sun, J. S. Francisco, M. Yang, Q. Huang and S. Du, *J. Phys. Chem. C*, 2018, **123**, 2691–2702.
49 W. Shi and E. J. Maginn, *J. Chem. Theory Comput.*, 2007, **3**, 1451–1463.
50 W. Shi and E. J. Maginn, *J. Comput. Chem.*, 2008, **29**, 2520–2530.
51 A. Rahbari, R. Hens, M. Ramdin, O. Moultos, D. Dubbeldam and T. J. H. Vlugt, *Mol. Simul.*, 2021, **47**, 804–823.
52 R. Hens, A. Rahbari, S. Caro-Ortiz, N. Dawass, M. Erdös, A. Poursaeidesfahani, H. S. Salehi, A. T. Celebi, M. Ramdin and O. A. Moultos, *et al.*, *J. Chem. Inf. Model.*, 2020, **60**, 2678–2682.
53 H. M. Polat, H. S. Salehi, R. Hens, D. O. Wasik, A. Rahbari, F. de Meyer, C. Houriez, C. Coquelet, S. Calero, D. Dubbeldam, O. A. Moultos and T. J. H. Vlugt, *J. Chem. Inf. Model.*, 2021, **61**, 3752–3757.
54 A. Z. Panagiotopoulos, N. Quirke, M. Stapleton and D. Tildesley, *Mol. Phys.*, 1988, **63**, 527–545.
55 A. Poursaeidesfahani, A. Torres-Knoop, D. Dubbeldam and T. J. H. Vlugt, *J. Chem. Theory Comput.*, 2016, **12**, 1481–1490.
56 A. Z. Panagiotopoulos and M. R. Stapleton, *Fluid Phase Equilib.*, 1989, **53**, 133–141.
57 A. Panagiotopoulos, *Fluid Phase Equilib.*, 1992, **76**, 97–112.
58 F. Wang and D. P. Landau, *Phys. Rev. Lett.*, 2001, **86**, 2050–2053.
59 A. Poursaeidesfahani, A. Torres-Knoop, D. Dubbeldam and T. J. H. Vlugt, *J. Chem. Theory Comput.*, 2016, **12**, 1481–1490.
60 A. Rahbari, A. Poursaeidesfahani, A. Torres-Knoop, D. Dubbeldam and T. J. H. Vlugt, *Mol. Simul.*, 2018, **44**, 405–414.
61 S. Lasala, K. Samukov, H. M. Polat, V. Lachet, O. Herbinet, R. Privat, J.-N. Jaubert, O. A. Moultos, K. De Ras and T. J. H. Vlugt, *Chem. Eng. J.*, 2024, **483**, 148961.
62 H. M. Polat, S. Lasala, F. De Meyer, C. Houriez, O. A. Moultos and T. J. H. Vlugt, *Fluid Phase Equilib.*, 2024, **582**, 114084.
63 N. Ferrando, V. Lachet and A. Boutin, *J. Phys. Chem. B*, 2010, **114**, 8680–8688.
64 J. S. Rowlinson and B. Widom, *Molecular theory of capillarity*, Courier Corporation, 3rd edn, 2013.
65 D. Frenkel and B. Smit, *Understanding molecular simulation: from algorithms to applications*, Elsevier, 3rd edn, 2023.
66 A. Tamir, C. Dragoescu, A. Apelblat and J. Wisniak, *Fluid Phase Equilib.*, 1983, **10**, 9–42.
67 C. Burrus and J. Graybeal, *Phys. Rev.*, 1958, **109**, 1553.

68 H. A. Lorentz, *Ann. Phys.*, 1881, **248**, 127–136.
69 T. Darden, D. York and L. Pedersen, *J. Chem. Phys.*, 1993, **98**, 10089–10092.
70 U. Essmann, L. Perera, M. L. Berkowitz, T. Darden, H. Lee and L. G. Pedersen, *J. Chem. Phys.*, 1995, **103**, 8577–8593.
71 H. M. Polat, F. de Meyer, C. Houriez, O. A. Moultos and T. J. H. Vlugt, *J. Chem. Theory Comput.*, 2023, **19**, 2616–2629.
72 F. Torrens, *Toxicol. Environ. Chem.*, 1999, **73**, 177–189.
73 C. M. Western, P. R. Langridge-Smith, B. J. Howard and S. E. Novick, *Mol. Phys.*, 1981, **44**, 145–160.
74 A. East, A. McKellar and J. Watson, *J. Chem. Phys.*, 1998, **109**, 4378–4383.
75 E. D. Glendening and A. M. Halpern, *J. Chem. Phys.*, 2007, **127**, 164307–164311.
76 A. Malakhovskii and A. Gedanken, *J. Chem. Soc., Faraday Trans.*, 1996, **92**, 329–332.
77 H. C. Shi, *Computational study of electronic excited states of nitric oxide monomer and nitric oxide dimer*, Faculty of Graduate Studies and Research, University of Regina, 2007.
78 M. W. Chase, *NIST-JANAF thermochemical tables*, American Chemical Society, Washington, DC, New York, 1998.
79 B. Howard and A. McKellar, *Mol. Phys.*, 1993, **78**, 55–72.
80 R. González-Luque, M. Merchán and B. O. Roos, *Theor. Chim. Acta*, 1994, **88**, 425–435.
81 A. Dkhissi, P. Soulard, A. Perrin and N. Lacome, *J. Mol. Spectrosc.*, 1997, **183**, 12–17.
82 M. Lsal, J. K. Brennan and W. R. Smith, *J. Chem. Phys.*, 2006, **124**, 064712–064725.
83 C. H. Turner, J. K. Johnson and K. E. Gubbins, *J. Chem. Phys.*, 2001, **114**, 1851–1859.
84 R. Rowley, W. Wilding, J. Oscarson, N. Zundel, T. Marshall, T. Daubert and R. Danner, *DIPPR Data Compilation of Pure Chemical Properties*, AIChE, 2010.
85 J. Pedley, *Thermochemical data and structures of organic compounds*, CRC Press, 1994, vol. 1.
86 N. Taguchi, Y. Mochizuki, T. Ishikawa and K. Tanaka, *Chem. Phys. Lett.*, 2008, **451**, 31–36.

 